Sigma vector calculations in nodal aberration theory and experimental validation using a Cassegrain telescope

MELTEM YEŞILTEPE, 1,2 AARON BAUER, 3 DÖZGÜR KARCI, 4,* DAND JANNICK P. ROLLAND³

Abstract: Nodal Aberration Theory (NAT) was developed to explain the field dependency of aberration field centers in the image plane of nominally rotationally symmetric optical systems that have lost their symmetry through misalignments. A new insight into the theory led to calculating the sigma vectors, which locate the aberration field centers, using the angle between a real-ray trace of the optical axis ray (OAR) and the normal of the local surface where "local" refers to the object and image optical spaces of that surface. Here, we detail the sigma vector calculations for general optical systems and provide an experimental investigation of a misaligned system with a high-precision customized Cassegrain telescope. In the simulations, a Newtonian telescope, a Cassegrain telescope, and a three-mirror anastigmat telescope were misaligned intentionally in ray-tracing software. The sigma vectors were calculated analytically for the third-order aberrations of astigmatism and coma. Experimentally, the same perturbations were implemented for the Cassegrain telescope system, and the aberrations were quantified through interferometric measurements on a grid of field points in the image plane that verified the analytical derivation and simulations.

© 2023 Optica Publishing Group under the terms of the Optica Open Access Publishing Agreement

1. Introduction

Nodal Aberration Theory (NAT) describes and quantifies the aberration properties of nominally rotationally symmetric optical systems that are misaligned. NAT builds upon H.H. Hopkins' scalar wave aberration theory [1] and R. Buchroeder's concept of the shifted aberration field centers on the image plane for misaligned optical systems [2]. The theory, invented by R.V. Shack, was developed up to the fifth order by K. P. Thompson and Shack [3–8]. Experimental investigations of NAT are still in progress. N. Zhao et al. first experimentally demonstrated field-constant coma for an aplanatic Ritchey-Chretien telescope [9]. Next, the experimental investigation of binodal astigmatism, which was the aberration field dependence that led to the discovery of NAT [10], was first experimentally validated for a customized Cassegrain telescope [11], followed by the validation of the separation of binodal astigmatism induced by mount error and misalignment [12], and field-linear coma for a Cassegrain telescope [13].

NAT predicts that the aberrations of misaligned optical systems show new field dependency and nodal behavior (i.e., where an aberration goes to zero), but there are no new aberration types. The exact locations of the aberration field centers or nodes in the image plane are determined by a weighted sum of the individual surface contributions in the optical system. For this purpose, Buchroeder developed a method based on paraxial ray-tracing for perturbations of small tilts and decenters [2]. Afterward, Thompson et al. put forth a new insight for locating the aberration field centers based on real-ray-trace data that is valid for any misalignments [14]. In this method,

¹TÜBİTAK Space Technologies Research Institute, METU Campus, 06800, Çankaya, Ankara, Turkey

 $^{^2}$ Gazi University, The Department of Advanced Technologies, 06500, Yenimahalle, Ankara, Turkey

³The Institute of Optics, University of Rochester, 275 Hutchison Road, Rochester, NY 14627, USA

⁴Turkish Aerospace Industries, 06980, Kahramankazan, Ankara, Turkey

^{*}ozgur.karci@tai.com.tr

sigma vectors to locate the aberration field centers were calculated using the angle between a real-ray trace of the optical axis ray (OAR) and the normal of the local surface. This angle is entirely free of how the misalignments are modeled and can be obtained from optical design software. This approach in NAT provides valuable insight to the optical designers, such as evaluating the alignment state of an optical system and the fruitfulness of the compensators in assembly.

Here, we review and detail the calculation of sigma vectors in NAT for a general optical system. The calculations are verified numerically using ray-tracing software for one, two, and three-mirror systems. Additional detail is provided for the two-mirror customized Cassegrain telescope design [15], and experimental investigations were conducted in parallel to the simulations for this system. The remainder of this paper is organized as follows. Section 2 reviews the computational method for the sigma vectors. Section 3 provides the theoretical background of NAT, including third-order aberrations that show nodal behavior in the image plane. The analytical node positions are verified using numerically calculated nodes in Section 4. Section 5 provides paraxial quantities for the customized Cassegrain telescope, calculations of surface aberration coefficients, and a detailed description of the experimental setup. Section 6 presents the results of sigma vector calculations for coma and astigmatism and compares the theory and experiments.

2. Sigma vectors

In optical systems with rotational symmetry, the OAR, defined as the ray that connects the center of the object plane and the center of the aperture stop, coincides with the Mechanical Axis (MCA), which is used for calculating paraxial and third-order quantities of the optical system. In that case, the OAR also intersects all centers of curvatures and vertices of the surfaces and the center of the image plane. In an optical system with symmetry, the incident angle of the OAR at each surface is always zero; thus, the field displacement vectors are zero.

With misalignments, the intersection point of the OAR and the image plane becomes a new center of the field. The shift of the MCA from this new field center is called the boresight error. The boresight error for a two-mirror telescope system whose aperture stop is located at the primary mirror is shown in Fig. 1(a).

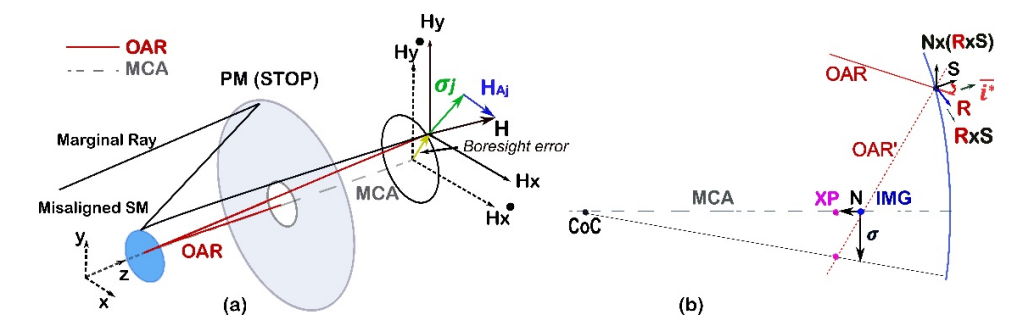


Fig. 1. (a) The image plane field coordinates for the aligned and misaligned cases are denoted by and $H_{x,y}$, respectively. The sigma vector is σ_j , H is the field vector for the unperturbed system, and H_{Aj} is the effective field vector after misalignment. (b) Demonstration of N, R, and S vectors at the j^{th} surface. The line labeled OAR' represents the optical axis ray after reflection. CoC, XP, and IMG points represent the center of curvature, exit pupil location, and image location, respectively.

Furthermore, with misalignments, the center of symmetry for a given aberration contribution for a perturbed surface, *j*, shifts to another point in the local image plane, which will also map to a new aberration center in the final image plane. This field displacement vector is called a sigma

vector and is denoted by σ_j [14] (where bold depicts vector). The sigma vector starts at the intersection point of the OAR and the image plane. In NAT, if a surface is aspheric, two separate sigma vectors have to be calculated, one originating from the spherical base curve and the second one originating from the aspheric departure from the spherical surface [14]. Therefore, the sigma vector consists of two components: one from the spherical contribution and the other from the aspherical contribution if an asphere is used. Here, a simple conic would fall under an aspherical contribution.

The spherical contribution of the sigma vector was previously computed by Buchroeder [2]. He developed a method based on paraxial ray trace equations, accounting for surface tip/tilt parameters. In his method, the OAR is parameterized by $u_{OAR}^{\#}$ (inclination angle at the surface) and $\bar{y}_{OAR}^{\#}$ (intersection height at the surface), parameters measured from the MCA. The drawback of this method was that it could not be easily implemented in a commercial design program [14,16]. Then, the coordinate-independent method of Thompson *et al.* was developed that allows computing the spherical contribution of the sigma vector based on real-ray trace data. The equation for computing the spherical contribution of the sigma vector of a misaligned surface is given as [14]

$$\sigma_j^{sph} = -\frac{\overline{i^*}}{\overline{i_j}} = \frac{-N_j \times (R_j \times S_j)}{\overline{i_j}},$$
(1)

where the subscript j is used to define a subjected surface, \overline{i}^* is the angle of incidence of the OAR at the surface, $\overline{i_j}$ is the local angle of incidence of the paraxial chief ray to use for normalization to image height and N_j , R_j , and S_j are all unit vectors with normalized direction cosines of (X, Y, Z), (L, M, N), and (SRL, SRM, SRN), respectively. Note that * denotes parameters related to the OAR. N_j is the normal vector of the object/image plane for the unperturbed system, perpendicular to the Z-axis. R_j is the normalized direction vector along the incident ray OAR. S_j is the vector along the surface normal at the intersection of the OAR and the surface. An example of the N_j R_j , and S_j vectors at a surface were given in Fig. 1(b). Note that the N vector is taken to point from the local image point towards the local exit pupil.

The aspheric contribution of the sigma vector depends on the intersection height of the OAR relative to the aspherical vertex and is computed by [14]

$$\sigma_j^{asph} = \frac{\delta v^*}{\overline{y_j}},\tag{2}$$

where, δv^* is the aspheric vertex departure of the OAR from the MCA, and $\overline{y_j}$ is the chief ray height at the surface.

Since NAT is a surface-based theory, the contribution of a specific surface to the net aberration field is distinguishable and identifiable, and we are currently exploring techniques to achieve this goal. NAT applies to both reflective and refractive optical systems. For instance, if a lens is misaligned, that results in both surfaces of that lens being misaligned. Each surface of the lens is treated separately, but the misalignment values of each surface are understandably tied together. The final sigma vector has contributions from each surface of the lens. In addition, asymmetric systems consisting of off-axis components can be analyzed using the same formalism as for rotationally symmetric systems discussed. The difference is that each component of an asymmetric system would have some purposeful "misalignment" that describes its position in space. Furthermore, some concepts from NAT have been borrowed to explain how non-symmetric optical elements (i.e., freeform) impact the net aberration field, leading to major advances in the design, fabrication, testing, and assembly of freeform systems [17–19]. The effect of the surface figure errors on the aberrations is also explained by NAT successfully [12,20], but it is not the focus of this study.

3. Analytical calculations for the third-order node locations

The general vector form of the wavefront aberration expansion is expressed as

$$W = \sum_{j} \sum_{p}^{\infty} \sum_{n}^{\infty} \sum_{m}^{\infty} (W_{klm})_{j} (\boldsymbol{H}.\boldsymbol{H})^{p} (\boldsymbol{\rho}.\boldsymbol{\rho})^{n} (\boldsymbol{H}.\boldsymbol{\rho})^{m},$$
(3)

where H and ρ are normalized field and aperture vectors, respectively, and $(W_{klm})_j$ are the aberration coefficients of the surface j. For an optical system without symmetry, with the inclusion of the sigma vector contribution to the field vector of an unperturbed optical system, we obtain the new field dependency of aberrations as

$$H_{Aj} = H - \sigma_j \tag{4}$$

where H_{Aj} is the effective field vector. Rewriting the wave aberration expansion to comprise only third-order aberrations yields

$$W = \sum_{j} W_{040j}(\boldsymbol{\rho}.\boldsymbol{\rho})^{2} + \sum_{j} W_{131j}[(\boldsymbol{H} - \boldsymbol{\sigma}_{j}).\boldsymbol{\rho}](\boldsymbol{\rho}.\boldsymbol{\rho}) + \sum_{j} W_{222j}[(\boldsymbol{H} - \boldsymbol{\sigma}_{j}).\boldsymbol{\rho}]^{2}$$

$$+ \sum_{j} W_{220Sj}[(\boldsymbol{H} - \boldsymbol{\sigma}_{j}).(\boldsymbol{H} - \boldsymbol{\sigma}_{j})](\boldsymbol{\rho}.\boldsymbol{\rho}) + \sum_{j} W_{311j}[(\boldsymbol{H} - \boldsymbol{\sigma}_{j}).(\boldsymbol{H} - \boldsymbol{\sigma}_{j})][(\boldsymbol{H} - \boldsymbol{\sigma}_{j}).\boldsymbol{\rho}]$$
(5)

where W_{040} , W_{131} , W_{222} , W_{220} , and W_{311} are the aberration coefficients that represent third-order spherical aberration, coma, astigmatism, field curvature, and distortion, respectively.

3.1. Coma node location

In optical systems without symmetry, third-order coma can have up to one node in the image plane. To compute the coma node location, we first sum the sigma vectors of the individual surfaces weighted by the corresponding surface aberration contributions for coma given by [5]

$$A_{131} = \sum_{j} (W_{131,j}{}^{sph} \sigma_{j}{}^{sph} + W_{131,j}{}^{asph} \sigma_{j}{}^{asph}), \tag{6}$$

where A_{131} is an un-normalized vector in the image plane. $W_{131,j}{}^{sph}$ and $W_{131,j}{}^{asph}$ are spherical and aspherical aberration contributions of surface j, respectively. $\sigma_j{}^{sph}$ and $\sigma_j{}^{asph}$ are spherical and aspherical sigma vectors contributions of surface j, respectively. If the system-level third-order coma aberration is non-zero, A_{131} can be normalized by system-level W_{131} as

$$a_{131} \equiv \frac{A_{131}}{W_{131}} \ . \tag{7}$$

The a_{131} vector points to the coma node in the normalized field coordinates. The coma node locations for aligned and misaligned states are depicted in Fig. 2(a) and Fig. 2(b), respectively.

3.2. Astigmatism nodes locations

In optical systems without symmetry, third-order astigmatism can have up to two nodes in the image plane. To compute astigmatism node locations, we first sum the sigma vectors of the individual surfaces weighted by the corresponding surface aberration contributions for astigmatism to yield the displacement vector A_{222} given as [5],

$$A_{222} = \sum_{j} (W_{222,j}{}^{sph} \sigma_{j}{}^{sph} + W_{222,j}{}^{asph} \sigma_{j}{}^{asph}), \qquad (8)$$

where $W_{222,j}^{sph}$ and $W_{222,j}^{asph}$ are the spherical and aspherical aberration contributions of surface j, respectively. Similarly, we then form another vector \mathbf{B}_{222}^2 related to the Shack vector product

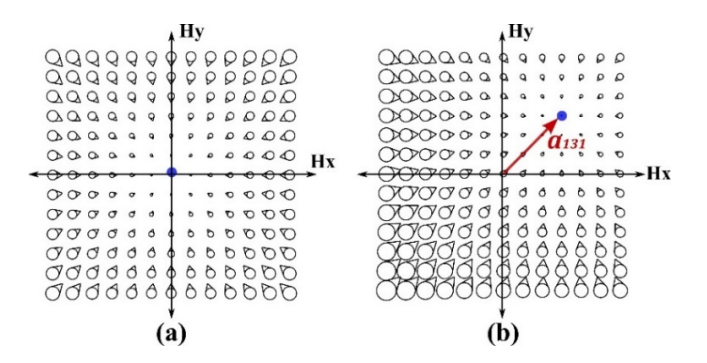


Fig. 2. Full Field Displays (FFDs) of the third-order coma $(Z_{7/8})$ for a Cassegrain telescope and the node locations for (a) an aligned state where a_{131} is zero, (b) a misaligned state.

[21,22] of the sigma vectors with themselves in a weighted sum given as [5]

$$\boldsymbol{B}_{222}^{2} = \sum_{j} (W_{222,j}{}^{sph}\boldsymbol{\sigma}_{j}{}^{sph^{2}} + W_{222,j}{}^{asph}\boldsymbol{\sigma}_{j}{}^{asph^{2}}), \tag{9}$$

If we consider the system-level astigmatism for the aligned system, W_{222} , to be non-zero, the normalization of the A_{222} vector is given as [5]

$$a_{222} \equiv \frac{A_{222}}{W_{222}} \tag{10}$$

where a_{222} is a normalized vector in field coordinates. Similarly, a normalized vector b_{222}^2 is composed of the B_{222}^2 vector divided by W_{222} , and an additional term that is the Shack vector product of a_{222} with itself (i.e., a_{222}^2), given as [5]

$$\boldsymbol{b}_{222}^2 \equiv \frac{\boldsymbol{B}_{222}^2}{W_{222}} - \boldsymbol{a}_{222}^2,\tag{11}$$

Isolating the astigmatism and field curvature terms from Eq. (5), referencing the medial focal plane, and integrating Eq. (10) and Eq. (11), astigmatism may be expressed as [5]

$$W = \frac{1}{2}W_{222}[(\mathbf{H} - \mathbf{a}_{222})^2 + \mathbf{b}_{222}^2]. \ \boldsymbol{\rho}^2. \tag{12}$$

This new characteristic field dependence for astigmatism in the optical system can be solved according to the Shack vector product for locations where the astigmatic terms go to zero for \mathbf{H} as [5]

$$0 = (\mathbf{H} - \mathbf{a}_{222})^2 + \mathbf{b}_{222}^2. \tag{13}$$

The vectors \mathbf{a}_{222} , and $\pm i\mathbf{b}_{222}$ comprise a vector from the center of the field to the midpoint between two astigmatic nodes and two vectors pointing from the endpoint of the \mathbf{a}_{222} vector to the two astigmatic nodes, respectively, illustrated in Fig. 3(b), compared to the one centered node for an aligned system shown in Fig. 3(a).

As noted above and in earlier work [5,11], the solutions to Eq. (13) correspond to the field coordinate location of the astigmatism nodes. In this paper, our goal is to determine these same node locations directly as vector components, which avoid the need for imaginary numbers, thus simplifying the calculations for simulations and experimental data. To compute astigmatism

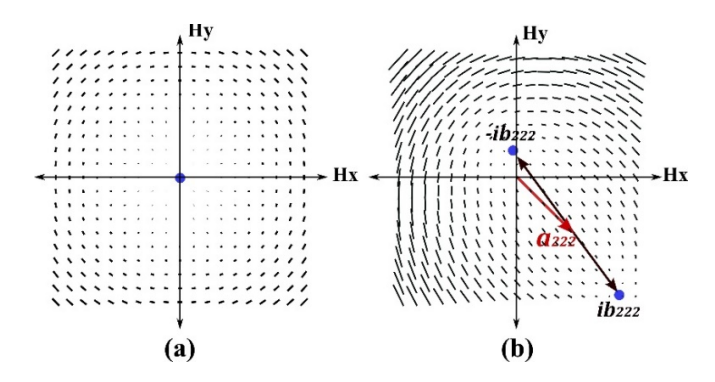


Fig. 3. Full Field Displays (FFDs) of third-order astigmatism $(Z_{5/6})$ for a Cassegrain telescope and the node locations: (a) for the aligned state ($a_{222} = 0$), (b) for a misaligned state.

node locations in component form, expressions given in Eq. (13) will be rewritten by using components of vectors as given below,

$$\boldsymbol{H} = \langle x_0 , y_0 \rangle \boldsymbol{a}_{222} = \langle a_x , a_y \rangle \boldsymbol{b}_{222}^2 = \langle b_x , b_y \rangle$$
 (14)

Substituting the above expressions into Eq. (13), we get,

$$0 = (\langle x_0, y_0 \rangle - \langle a_x, a_y \rangle)^2 + \langle b_x, b_y \rangle.$$
 (15)

To compute the square operation given in round brackets in Eq. (15), the Shack Vector Product will be used, resulting in

$$-\langle b_x, b_y \rangle = \langle 2(x_0 - a_x)(y_0 - a_y), (y_0 - a_y)^2 - (x_0 - a_x)^2 \rangle.$$
 (16)

Subsequently, by setting components placed on the right and the left sides of the equation, we get two equations to solve for x_0 and y_0 ,

$$-b_x = 2(x_0 - a_x)(y_0 - a_y)$$

$$-b_y = (y_0 - a_y)^2 - (x_0 - a_x)^2.$$
(17)

Solving the first equation of Eq. (17) for x_0 , we obtain,

$$x_0 = \frac{-b_x}{2(y_0 - a_y)} + a_x . ag{18}$$

Equation (18) is then substituted into the second equation in Eq. (17) to get

$$-b_y = \left(y_0^2 - 2y_0 a_y + a_y^2\right) - \left(\frac{-b_x}{2(y_0 - a_y)}\right)^2.$$
 (19)

Solving Eq. (19) for y_0 , we get four solutions below as Eq. (20-21). The two solutions in Eq. (21) always result in imaginary numbers due to $|b_y| \le \sqrt{b_x^2 + b_y^2}$, regardless of the sign of b_y . Thus, the two solutions corresponding to the two nodes in the astigmatism field are given by Eq. (20).

$$y_0 = a_y \pm \frac{\sqrt{-b_y + \sqrt{b_x^2 + b_y^2}}}{\sqrt{2}}$$
 (20)

$$y_0 = a_y \pm \frac{\sqrt{-b_y - \sqrt{b_x^2 + b_y^2}}}{\sqrt{2}} \tag{21}$$

4. Numerical verification of analytical node calculations

The analytical calculation for the location of the nodes of third-order coma and astigmatism in Section 3 is verified here using features of commercial ray-tracing software for one, two, and three-mirror systems, each with some misalignment applied to an optical surface. Using a custom MATLAB code to communicate with ray-tracing software, the optical model's relevant parameters required to calculate the node positions are extracted from each system [23]. Then, the analytical node positions are calculated as described in Section 3. We then use the ray-tracing software to numerically create a Full Field Display (FFD) that shows the orientation and magnitude of an aberration over a prescribed full field-of-view (FFOV). The aberration vs. FFOV data created in the generation of the FFD is used to numerically solve for the location of the aberration nodes. The analytical location and the numerical location of each node are then compared to verify the accuracy of the analytical calculation. We demonstrated this process for three systems: a Newtonian telescope, a Cassegrain telescope, and a three-mirror anastigmat. A system drawing and the resulting FFDs for coma and astigmatism are shown in Fig. 4. In each FFD, the red circles indicate the analytical nodes and the red crosses indicate the numerically solved nodes. There is close agreement between the theory and simulation for all three cases. Note that the decenter and tilt used in the misalignment for the Cassegrain telescope was a coma-free pivot point, also correctly predicted by the theory.

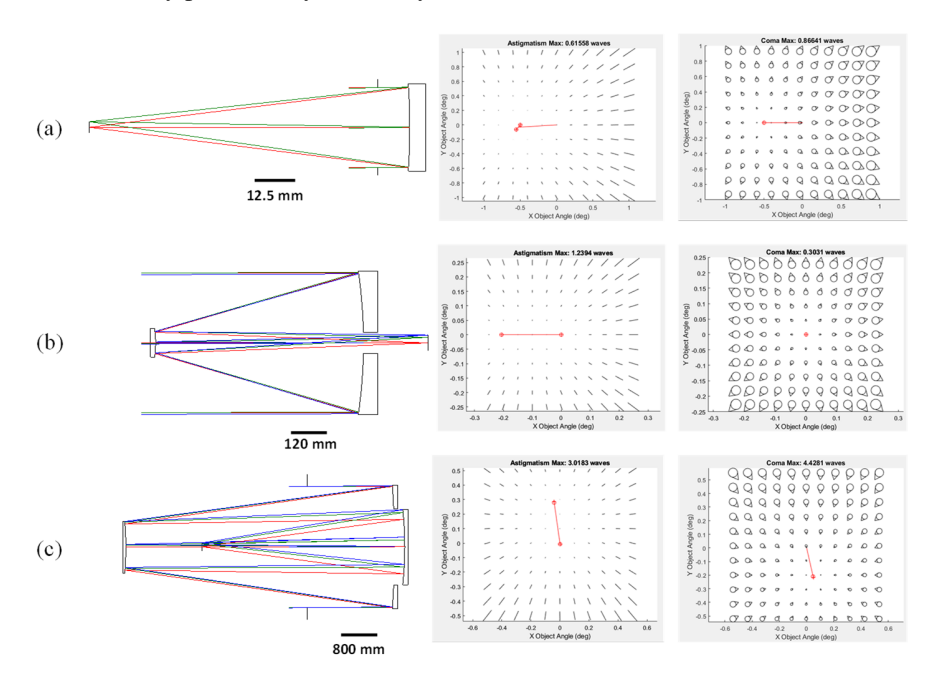


Fig. 4. Numerical verification of the analytical node location calculations computed for (a) a one-mirror Newtonian telescope, (b) a two-mirror Cassegrain telescope, and (c) a three-mirror anastigmat telescope. Each red cross in the FFDs indicates the location of a numerically solved node, and the red circles indicate the location of the analytically computed nodes.

It is important to note that since the analytical calculation is only valid for third-order aberrations, optical systems with non-negligible contributions of fifth and higher orders of aberrations are not appropriate to use for numerical verification. The real-ray based FFDs used to generate the numerical data are ordered agnostic and, thus, show all orders of aberrations.

System-level specifications for each of the three systems are provided in Appendix A, including the applied misalignments (Table 10).

5. Example application of sigma vectors for a two-mirror telescope

To further demonstrate the theory's application in Sections 2 and 3, we look at the two-mirror Cassegrain telescope more deeply. The system will be misaligned intentionally. We then compute the node locations analytically and significantly, confirming the findings for the zeros in the aberration fields experimentally.

5.1. Cassegrain telescope design

A Ø490 mm aperture, F/12.7, high-precision Cassegrain telescope was used for simulations and was fabricated for the experimental investigation of sigma vectors. The Cassegrain telescope comprises a parabolic concave primary mirror, set as the aperture stop in design, and a hyperbolic convex secondary mirror. The telescope is designed to have diffraction-limited performance over a \pm 0.11-degree FFOV. The telescope optical prescription is listed in Table 1. The design was optimized with a reference wavelength of 632.8 nm, matching the experiment's wavelength.

Surface Surface Type Radius of Curvature Thickness Refract Mode Conic Constant (mm) (mm) OBJECT Plane Infinity Refract 0 PM -1700-720.575Reflect -1.000Conic SM Conic -300943.887 Reflect -1.737Refract 0 **IMAGE** Plane

Table 1. Optical prescription of the Cassegrain telescope.

5.2. Calculations of the third-order aberration coefficients

This section uses paraxial ray-trace data to calculate the primary and secondary mirrors' third-order astigmatism and coma aberration contributions. Using the optical prescription given in Table 1, the paraxial ray-trace data, which is also used for the sigma vector calculations, is gathered through the ray-tracing software and is given in Table 2. The third-order aberration coefficients were calculated using this paraxial data (Appendix B, Table 11, Table 12, Table 13, Table 14) and shown in Table 3.

Table 2. Paraxial ray-tracing data for the Cassegrain telescope

Surface	y (mm)	u (deg.)	$\bar{y}(mm)$	ū (deg.)
EP	245.000000	0	0	0.004363
PM	245.000000	0.288235	0	-0.004363
SM	37.304364	-0.039515	3.144125	0.0253262
IMG	0.006349	-0.039515	27.049246	0.0253262

Table 3. Aberration surface contributions for third-order astigmatism and coma aberrations

Aberration Contr.	W_{222}^{sph}	W_{222}^{asph}	W_{222}	W_{131}^{sph}	W_{131}^{asph}	W_{131}
PM (in waves)	1.06233	0	1.06233	-35.08779	0	-35.08779
SM (in waves)	-1.61556	1.39900	-0.21656	17.83462	16.59885	34.43347

5.3. Analytical calculations and simulations

The misalignments given in Table 4 were introduced into the telescope's secondary mirror, and the relevant quantities were gathered for the sigma vector calculations. The secondary mirror was decentered along the X-axis and Y-axis and tilted around the X-axis and Y-axis. The spherical contributions of the surfaces' sigma vectors were calculated by Eq. (1). The direction cosines of the N, R, and S vectors were obtained by NASA Toolkit functions [24]. The computation results are given in Table 5. The parameters used to compute the aspherical contributions of the sigma vector are shown in Table 6.

Table 4. Employed perturbation quantities of the Cassegrain telescope.

Surface	XDE (mm)	YDE (mm)	ADE (deg.)	BDE (deg.)
SM	-0.250	0.500	-0.245	-0.095

Table 5. Quantities to compute the spherical contribution sigma vectors.

Parameters	Units	PM (Stop)	SM
l_i	mm	-∞	944.047693
l_{XP}	mm	0	-124.144736
X	none	0	0
Y	none	0	0
Z	none	1	-1
L	none	0	0.000009
M	none	0	0.000942
N	none	1	0.999999
SRL	none	0	-0.000833
SRM	none	0	0.001667
SRN	none	1	-0.999998
\bar{i}	none	-0.0043634	0.014845
σ_{x}^{sph}	none	0	0.055551
$oldsymbol{\sigma}_{\mathrm{y}}{}^{sph}$	none	0	-0.175777

Table 6. Quantities to compute the aspherical contribution sigma vectors.

Parameter	Units	PM (Stop)	SM
δv_x^*	mm	0	-0.249999
δv_y^*	mm	0	0.500004
	mm	0	3.144122
σ_{x}^{asph}	none	0	-0.079513
$oldsymbol{\sigma}_{ ext{y}}^{asph}$	none	0	0.159028

5.4. Experimental setup

The auto-collimation experimental setup consists of the Cassegrain telescope, a reference flat mirror, and an interferometer, as demonstrated in Fig. 5(a). A Fizeau phase-shifting interferometer with an F/10.7 transmission sphere is confocal to the telescope. The Ø800 mm aperture reference flat mirror with a motorized tip/tilt stage reflects the output light beam from the telescope.

The interferometer is placed on a five-axis manual stage that is used to align the focus of the interferometer onto each field point in the image plane. To align the secondary mirror, the telescope uses a customized, piezo-actuated, five-axis flexure mechanism. This mechanism is also used for introducing the misalignments into the telescope for this work. A schematic diagram of the experimental setup for the field measurements is shown in Fig. 5(b).

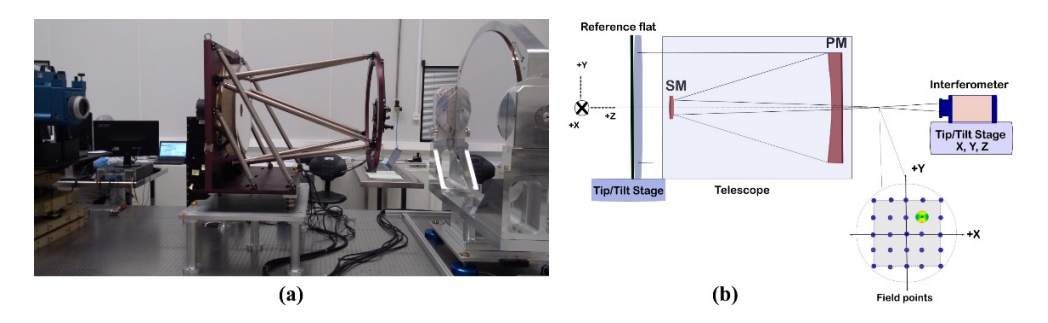


Fig. 5. Experimental setup: (a) Cassegrain telescope placed on the optical table in the auto-collimation setup configuration. (b) Schematic diagram of the experimental setup for the measurements. The Z-axis of the interferometer was fixed at the confocal point for the zero-field measurement, and it was not changed for the field measurements.

5.5. Experimental results and discussion

The misalignments given in Table 4 were introduced into the Cassegrain telescope for generating the aberrations. Then, the wavefront error (WFE) measurements were performed interferometrically on a 5×5 grid of field points, given in Table 7. The results of the raw interferometric measurement data (piston, tip/tilt are removed from the data) are presented in Fig. 6. In Fig. 6, interferometric data for the corner points were not accurate because of the inner diameter dimension limit of the primary mirror that caused obscuration for the interferometer beam. Therefore, the corner points were excluded from the calculations.

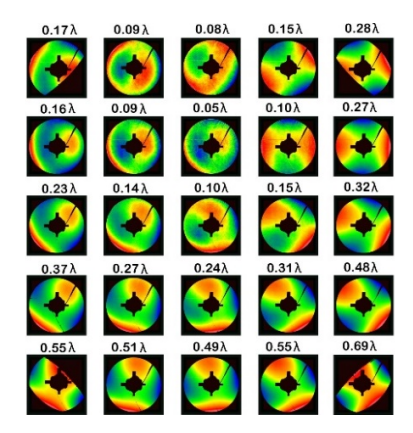


Fig. 6. Interferograms of the measurements for the misaligned state of the telescope (@ $\lambda = 632.8$ nm). The values on each data depict the RMS WFE for the field points.

In the next step, the third-order astigmatism $(Z_{5/6})$ and coma $(Z_{7/8})$ terms were extracted from the WFE data where $Z_{5/6}$ and $Z_{7/8}$ designate Zernike Fringe coefficients. The magnitudes of the third-order astigmatism and coma terms were calculated by $Z_{5/6} = \sqrt{Z_5^2 + Z_6^2}$ and

		•	J .	
(-0.250°, 0.250°)	(-0.125°, 0.250°)	(0°, 0.25°)	(0.125°, 0.250°)	(0.250°, 0.250°)
(-0.250°, 0.125°)	(-0.125°, 0.125°)	(0°, 0.125°)	(0.125°, 0.125°)	(0.250°, 0.125°)
(-0.250°, 0°)	(-0.125°, 0°)	(0°, 0°)	(0.125°, 0°)	(0.250°, 0°)
(-0.250°, -0.125°)	(-0.125°, -0.125°)	(0°, -0.125°)	(0.125°, -0.125°)	(0.250°, -0.125°)
(-0.250°, -0.250°)	(-0.125°, -0.250°)	(0°, -0.250°)	(0.125°, -0.250°)	(0.250°, -0.250°)

Table 7. 5×5 grid of field positions on the image plane simulated.

 $Z_{7/8} = \sqrt{Z_7^2 + Z_8^2}$, respectively. The simulated and experimental interferograms are illustrated in Fig. 7. As seen in Fig. 7(a), one of the third-order astigmatism nodes is located near the center of the FOV, and the second one is located close to the field point (-0.125, 0.250). As seen in Fig. 7(b), the third-order coma node is located between the field points (0.125, 0.250) and (0.125, 0.125). The interferograms obtained experimentally were also compared to the simulated interferograms in Fig. 7(c) and Fig. 7(d) to verify the specific aberrational behavior of third-order astigmatism and coma along the FOV.

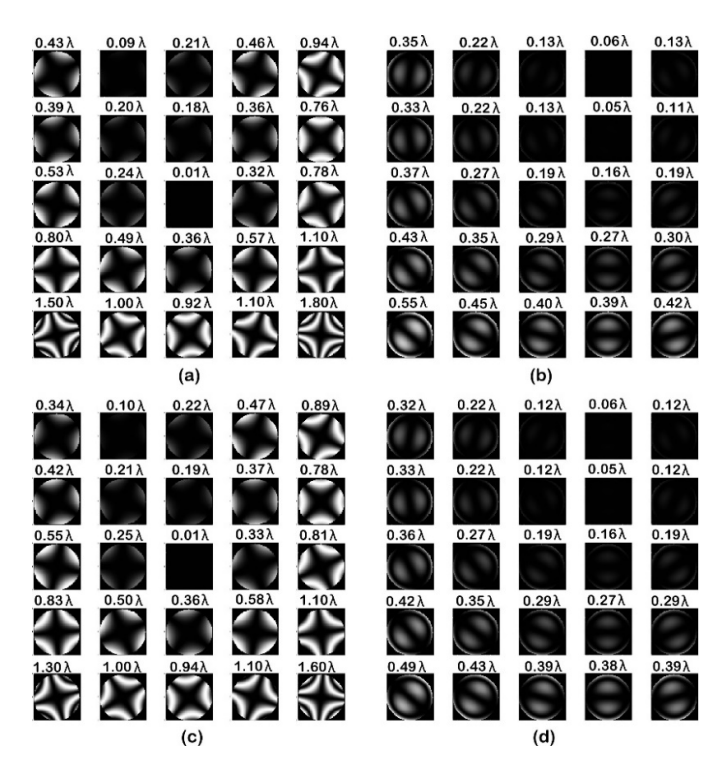


Fig. 7. Measured and simulated interferograms: (a) Experimental interferograms for third-order astigmatism $(Z_{5/6})$ and (b) third-order coma $(Z_{7/8})$ for the customized Cassegrain telescope. (c) Simulated interferograms for $Z_{5/6}$ and (d) $Z_{7/8}$ for the misaligned Cassegrain telescope.

The node locations were found by fitting the related Zernike Fringe coefficients, measured from field rows and columns around the nodes, to the appropriate polynomials concerning the field dependencies of the aberrations. The coma node location was directly determined as a result of the polynomial fitting process as the endpoint of the $a_{131} \times HFOV$ vector where HFOV designates

half field of view (i.e., 0.25-deg). The calculation of the components of the $a_{222} \times HFOV$ vector was performed by taking the midpoint of the astigmatism nodes. The results are given in Table 8.

Table 8. Calculated aberration field vectors for the misaligned state of the Cassegrain telescope.

Aberration field vectors	Simu	lation	Experir	nental
Adeitation field vectors	X-comp.	Y-comp.	X-comp.	Y-comp.
$(a_{222} - ib_{222}) \times HFOV$	-0.1165	0.3030	-0.1046	0.3021
$(\boldsymbol{a}_{222}+i\boldsymbol{b}_{222})\times HFOV$	-0.0023	-0.0036	-0.0141	-0.0039
$a_{222} \times HFOV$	-0.0594	0.1497	-0.0594	0.1491
$a_{131} \times HFOV$	0.1257	0.1891	0.1373	0.1811
a_{222}	-0.2376	0.5988	-0.2374	0.5964
a_{131}	0.5028	0.7564	0.5492	0.7244

After obtaining the a_{222} and a_{131} aberration field vectors experimentally, Eq. (9), and Eq. (13) were used to compute the sigma vectors contribution variables. Four equations were used to solve for $\sigma_{SM,x}^{sph}$, $\sigma_{SM,y}^{sph}$, $\sigma_{SM,x}^{asph}$, and $\sigma_{SM,y}^{asph}$. Then, the components of the sigma vector contributions were computed as given in Table 9. The experimental results are consistent with the computed analytical results presented in Table 9 within 1.63%. Hence, the experimental results validate the simulations and the analytical calculations predicted by NAT.

Table 9. Comparison of the calculated sigma vectors experimentally and by simulation

Sigma vectors	Simulation		Experimental	
contributions	X-comp.	Y-comp.	X-comp.	Y-comp.
$oldsymbol{\sigma}_{\mathit{SM}}{}^{\mathit{sph}}$	0.055551	-0.175776	0.054662	-0.174550
$oldsymbol{\sigma}_\mathit{SM}{}^{asph}$	-0.079513	0.159028	-0.080401	0.158988

To investigate the environmental effects such as air turbulence, vibration, and temperature on the stability of the interferometric measurements, a statistical analysis of the measurements was also carried out by performing multiple measurements on a single field point. In Fig. 8, nine measurements obtained from the field point [0.125, -0.250] are presented for three parameters

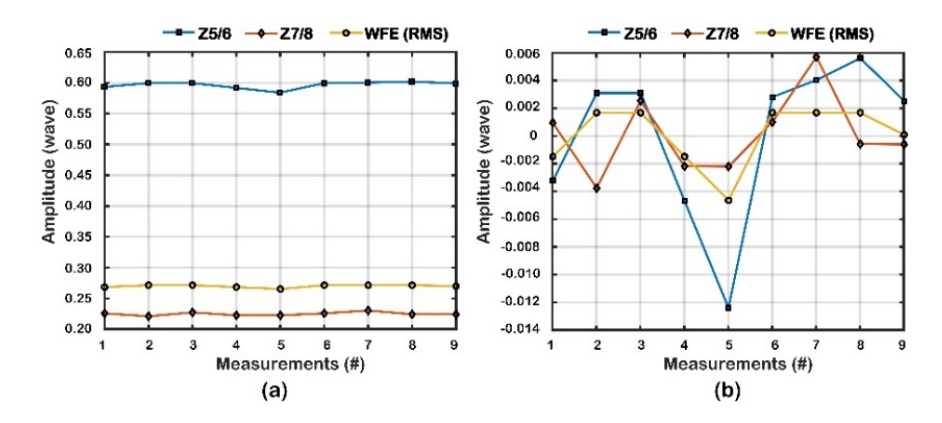


Fig. 8. (a) Statistical analysis of the measurements at the field point $(0.125^{\circ}, -0.250^{\circ})$ in the misaligned state of the telescope; (b) the deviation from the mean values shows nine consecutive measurements data for that field point in three different variables (@ λ = 632.8 nm).

of $Z_{5/6}$, $Z_{7/8}$, and RMS WFE. In Fig. 8(a), the amplitudes of measurements are depicted, and in Fig. 8(b), deviations from the average value for each measurement are demonstrated. The standard deviations for the $Z_{5/6}$, $Z_{7/8}$, and WFE (RMS) parameters are calculated to be 0.0058 λ , 0.0029 λ , and 0.0022 λ , respectively, which points to the extreme stability of the experimental setup.

6. Conclusion

In this work, we presented calculations for computing the sigma vectors in NAT, verified those calculations for one-, two-, and three-mirror telescopes, and experimentally validated the findings for a two-mirror telescope. The analytical calculations for a general optical system were presented in the first step. The sigma vectors for three misaligned telescopes were introduced in the second step using the given mathematical background simulations and analytical calculations. The simulations were validated experimentally on the Cassegrain telescope, whose secondary mirror was intentionally misaligned in the equivalent amount as presented in the simulations. In experiments, interferometric wavefront measurements were performed on twenty-one field points, and third-order astigmatism and coma were extracted from data to find the locations of the nodes. The sigma vectors were calculated experimentally after locating the nodes in the image plane. The simulations and analytical calculations agreed to within 1.63%, which validates the calculation of the sigma vectors in NAT for the first time.

The accuracy of the measurements was also checked by employing statistical analysis that confirmed that environmental effects did not limit the measurements. The primary source of error was the manual positioning of locating the interferometer focus on the field points. The study showed that sigma vectors in NAT are a powerful tool for the alignment of complex modern telescope systems as they can facilitate and expedite the telescope alignment. Generally, these telescope systems have large image planes. Field dependency-based diffraction-limited telescope alignment over the full image plane can be achieved by sigma vectors in a fast and accurate way. The investigation and experimentation of the inverse problem of utilizing the sigma vector for telescope alignment in a deterministic computer-aided procedure is an ongoing study and future standalone contribution. For future studies, new small-size interferometers with motorized stages can greatly expedite the whole measurement time. Moreover, point spread function (PSF) decomposition may be additionally used with a suitable experimental setup, extending the potential applications, such as measuring the telescope's image quality.

Appendix A: specifications for the systems used for verification in Section 4.

Parameter	Units	1-mirror	2-mirror	3-mirror
Focal length	mm	100	6196	10340
FFOV	deg	2	0.5	1
EPD	mm	25	490	2800
F-number	_	F/4	F/12.6	F/3.7
Perturbed surface	_	Primary	Secondary	Secondary
Perturbation amount	_	100 μm Y-Decenter 0.5° X-Tilt	-377 μm X-Decenter 0.167° X-Tilt (a coma-free pivot point)	1 mm X-Decenter 0.05° Y-Tilt

Table 10. Specifications for the systems used for verification in Section 4.

Appendix B: calculating third-order aberration coefficients from paraxial rays.

Table 11. First-order quantities.

Parameter	Description	Parameter	Description
у	Marginal ray height at a surface	R	Radius of curvature of a surface
\bar{y}	Chief ray height at a surface	t	Thickness after a surface
и	Marginal ray angle before a surface	k	Conic constant of a surface
u'	Marginal ray angle after a surface	A	Asphere coefficient of a surface
ū	Chief ray angle before a surface	l_o	Distance from a surface to the local object
\bar{u}'	Chief ray angle after a surface	l_i	Distance from a surface to the local image
n	Refractive index before a surface	l_{EP}	Distance from the surface to the local entrance pupil
n'	Refractive index after a surface	l_{XP}	Distance from the surface to the local exit pupil
i	Marginal ray angle of incidence	Ø	Optical power of a surface
\bar{i}	Chief ray angle of incidence	Н	Lagrange invariant

Table 12. Paraxial ray-tracing equations.

y at the next surface = $y + n'u' \frac{t}{n'}$	$i = u + \frac{y}{R}$	$l_{EP} = -\frac{\bar{y}}{\bar{u}}$
\bar{y} at the next surface = $\bar{y} + n'\bar{u}'\frac{t}{n'}$	$\bar{i} = \bar{u} + \frac{\bar{y}}{R}$	$l_{XP} = -\frac{\bar{y}}{\bar{u}'}$
$n'u' = n u - y \emptyset$	$l_o = -\frac{y}{u}$	$H = n\bar{u}y - nu\bar{y}$
$n'\bar{u}' = n \bar{u} - \bar{y}\emptyset$	$l_i = -\frac{y}{u'}$	$\emptyset = \frac{(n'-n)}{R}$

Table 13. Third-order coefficients [25].

Spherical coefficient	Aspherical coefficient
$S_{I,sph} = -\frac{1}{8} (ni)^2 \left(\frac{u'}{n'} - \frac{u}{n} \right) y$	$S_{I,asph} = A(n'-n)y^4 + \frac{1}{8R^3}k(n'-n)y^4$

Table 14. Third-order astigmatism and coma contributions.

Third-order astigmatism contributions	Third-order coma contributions
$W_{222}^{sph} = 4\left(\frac{\bar{i}}{\bar{i}}\right)^2 S_{I,sph}$	$W_{131}^{sph} = 4\left(\begin{array}{c} \bar{i} \\ \bar{i} \end{array}\right) S_{I, sph}$
$W_{222}^{asph} = 4\left(\frac{\bar{y}}{y}\right)^2 S_{I,asph}$	$W_{131}^{asph} = 4\left(\frac{\bar{y}}{y}\right) S_{I, asph}$

Funding. Fulbright (FY-2019-TR-PD-06).

Acknowledgments. Özgür Karcı thanks the Fulbright Commission for their partial support and the University of Rochester for their hosting during his Fulbright fellowship and continued collaboration on experimentally validating NAT. Özgür Karcı also thanks Mustafa Ekinci and Eray Arpa of TÜBİTAK. This research is synergistic with the National Science Foundation I/UCRC Center for Freeform Optics (IIP-1822049 and IIP-1822026).

Disclosures. The authors declare no conflicts of interest.

Data Availability. Data underlying the results presented in this paper are not publicly available at this time but may be obtained from the authors upon reasonable request.

References

- 1. H. H. Hopkins, Wave Theory of Aberrations (Oxford on Clarendon Press, 1950).
- 2. R. A. Buchroeder, Tilted Component Optical Systems (The University of Arizona, 1976).
- 3. K. P. Thompson, Aberration fields in tilted and decentered optical systems, (The University of Arizona, 1980).
- R. V. Shack and K. Thompson, "Influence of alignment errors of a telescope system on its aberration field," 251, 146–153 (1980).

- K. Thompson, "Description of the third-order optical aberrations of near-circular pupil optical systems without symmetry," J. Opt. Soc. Am. A 22(7), 1389–1401 (2005).
- K. P. Thompson, "Multinodal fifth-order optical aberrations of optical systems without rotational symmetry: spherical aberration," J. Opt. Soc. Am. A 26(5), 1090–1100 (2009).
- K. P. Thompson, "Multinodal fifth-order optical aberrations of optical systems without rotational symmetry: the comatic aberrations," J. Opt. Soc. Am. A 27(6), 1490–1504 (2010).
- K. P. Thompson, "Multinodal fifth-order optical aberrations of optical systems without rotational symmetry: the astigmatic aberrations," J. Opt. Soc. Am. A 28(5), 821–836 (2011).
- N. Zhao, J. C. Papa, K. Fuerschbach, Y. Qiao, K. P. Thompson, and J. P. Rolland, "Experimental investigation in nodal aberration theory (NAT) with a customized Ritchey-Chrétien system: third-order coma," Opt. Express 26(7), 8729–8743 (2018).
- J. P. Rolland, A. Bauer, K. Fuerschbach, T. Schmid, and K. P. Thompson, "Roland V. Shack's discovery of nodal aberration theory, the expansion into the aberrations of freeform optics, and impact in optical design," 11479, 11479 G (2020).
- Ö. Karcı, E. Arpa, M. Ekinci, and J. P. Rolland, "Experimental investigation of binodal astigmatism in nodal aberration theory (NAT) with a Cassegrain telescope system," Opt. Express 29(13), 19427–19440 (2021).
- Ö. Karcı, M. Yeşiltepe, E. Arpa, Y. Wu, M. Ekinci, and J. P. Rolland, "Experimental investigation in nodal aberration theory (NAT): separation of astigmatic figure error from misalignments in a Cassegrain telescope," Opt. Express 30(7), 11150–11164 (2022).
- Ö. Karcı, "A simulation and experimental validation of third-order coma in nodal aberration theory with a Cassegrain telescope," Turk. J. Phys. 45(6), 378–389 (2021).
- K. P. Thompson, T. Schmid, O. Cakmakci, and J. P. Rolland, "Real-ray-based method for locating individual surface aberration field centers in imaging optical systems without rotational symmetry," J. Opt. Soc. Am. A 26(6), 1503–1517 (2009).
- 15. Ö. Karcı and M. Ekinci, "Design of a high-precision, 0.5 m aperture Cassegrain collimator," Appl. Opt. **59**(27), 8434–8442 (2020).
- K. Thompson and J. Rolland, "A page from "the drawer": How Roland Shack opened the door to the aberration theory of freeform optics," Proc. SPIE 9186, 91860A (2014).
- K. Fuerschbach, J. P. Rolland, and K. P. Thompson, "Theory of aberration fields for general optical systems with freeform surfaces," Opt. Express 22(22), 26585–26606 (2014).
- A. Bauer, E. M. Schiesser, and J. P. Rolland, "Starting geometry creation and design method for freeform optics," Nat. Commun. 9(1), 1756 (2018).
- J. P. Rolland, M. A. Davies, T. J. Suleski, C. Evans, A. Bauer, J. C. Lambropoulos, and K. Falaggis, "Freeform optics for imaging," Optica 8(2), 161–176 (2021).
- T. Schmid, J. P. Rolland, A. Rakich, and K. P. Thompson, "Separation of the effects of astigmatic figure error from misalignments using Nodal Aberration Theory (NAT)," Opt. Express 18(16), 17433 (2010).
- R. W. Gray and J. P. Rolland, "Wavefront aberration function in terms of RV Shack's vector product and Zernike polynomial vectors," J. Opt. Soc. Am. A 32(10), 1836–1847 (2015).
- 22. D. Hestenes, "Oersted Medal Lecture 2002: Reforming the mathematical language of physics," Am. J. Phys. **71**(2), 104–121 (2003).
- Nodal Aberration Theory Sigma Vector Calculator (https://www.mathworks.com/matlabcentral/fileexchange/<...>),
 MATLAB Central File Exchange. Retrieved August 4, 2023.
- 24. "MATLAB-Zemax Toolkit (GSC-15151-1) NASA Software Catalog," retrieved https://software.nasa.gov/software/GSC-15151-1.
- 25. J. M. Sasian, "How to approach the design of a bilateral symmetric optical system," Opt. Eng. 33(6), 2045–2061 (1994).